Mon. Not. R. Astron. Soc. **000**, 1–16 (2014) Printed 23 October 2014 (MN LATEX style file v2.2)

Gas around galaxy haloes: methodology comparisons using hydrodynamical simulations of the intergalactic medium

Avery Meiksin[1⋆], James S. Bolton[2], Eric R. Tittley[1]
[1] *SUPA†, Institute for Astronomy, University of Edinburgh, Blackford Hill, Edinburgh EH9 3HJ, UK*
[2] *School of Physics and Astronomy, University of Nottingham, University Park, Nottingham NG7 2RD, UK*

arXiv:1410.5812v1 [astro-ph.CO] 21 Oct 2014

Accepted . Received ; in original form

ABSTRACT

We perform cosmological simulations of the intergalactic medium (IGM) at redshift $z \sim 3$ using the numerical gravity-hydrodynamics codes `GADGET-3` and `Enzo` for the purpose of modelling the gaseous environments of galaxies. We identify haloes in the simulations using three different algorithms. Different rank orderings of the haloes by mass result, introducing a limiting factor in identifying haloes with observed galaxies. We also compare the physical properties of the gas between the two codes, focussing primarily on the gas outside the virial radius, motivated by recent HI absorption measurements of the gas around $z \sim 2$–3 galaxies. The internal dispersion velocities of the gas in the haloes have converged for a box size of 30 comoving Mpc, but the centre-of-mass peculiar velocities of the haloes have not up to a box size of 60 comoving Mpc. The density and temperature of the gas within the instantaneous turn-around radii of the haloes are adequately captured for box sizes 30 Mpc on a side, but the results are highly sensitive to the treatment of unresolved, rapidly cooling gas, with the gas mass fraction within the virial radius severely depleted by star formation in the `GADGET-3` simulations. Convergence of the gas peculiar velocity field on large scales requires a box size of at least 60 Mpc. Outside the turn-around radius, the physical state of the gas agrees to 30 percent or better both with box size and between simulation methods. We conclude that generic IGM simulations make accurate predictions for the intergalactic gas properties beyond the halo turn-around radii, but the gas properties on smaller scales are highly dependent on star formation and feedback implementations.

Key words: cosmology: large-scale structure of Universe – methods: N-body simulations

1 INTRODUCTION

The gaseous environments of forming galaxies are expected to be a maelstrom of activity. Gaseous flows into dark matter haloes feed galaxies with material for creating stars. The resulting supernovae drive outflows that may impede or disrupt the inflow. These outflows may have several consequences on the growth of galaxies and their gaseous environments. They may regulate star formation in the galaxies, open up pathways for the release of ionizing photons that contribute to the metagalactic photoionization background, and possibly distribute metals over intergalactic scales.

Observational evidence for outflows in moderate redshift ($1.5 \lesssim z \lesssim 3$) galaxies has been mounting for over a decade. Spectral measurements of star-forming galaxies reveal blue-shifted metal absorption lines, sometimes accompanied by enhanced blue Balmer emission wings or red-shifted Lyα emission (e.g. Steidel et al. 1996; Franx et al. 1997; Pettini et al. 2000, 2001; Weiner et al. 2009; Steidel et al. 2010; Quider et al. 2010; Genzel et al. 2011). While mass flow rate estimates are fraught with uncertainties, the absorption and velocity signatures suggest outflow rates comparable to the star formation rates of the galaxies, with a large reservoir of cool gas built up by the outflows in the circumgalactic region (Steidel et al. 2010; Genzel et al. 2011).

On the other hand, evidence for cold, inflowing gas has been less forthcoming. Inflows may either arise from cosmological accretion onto the haloes, or by returning gas carried outward earlier by winds. Detection of the inflow patterns around moderate redshift ($z = 2 - 3$) galaxies has, how-

⋆ E-mail: A.Meiksin@ed.ac.uk (AM)
† Scottish Universities Physics Alliance

© 2014 RAS

ever, recently been provided by velocity measurements of the Lyα optical depth of neutral hydrogen in the vicinity of galaxies (Rakic et al. 2012; Rudie et al. 2012), extending from circumgalactic scales out to several comoving Mpc.

Feedback in the form of winds driven by supernovae have long been suspected of regulating the inflow and outflow of gas around galaxy haloes (Mathews & Baker 1971; Larson 1974). The gravitational influence of dark matter will favour mass loss via winds from low mass haloes over large, and may be responsible for the distinction between dwarf and normal galaxies (Dekel & Silk 1986). The ram pressure of cosmological accretion onto sufficiently massive haloes may even trap a wind within the turn-around radius, where the gas has decoupled from the Hubble expansion and is inflowing, leading to renewed infall and star formation (Fujita et al. 2004).

Given the variety of complex, non-linear physical mechanisms at play in the gaseous environments of galaxy haloes, cosmological hydrodynamical simulations are widely used to model the observational data. However, although many simulations with winds have been performed, the basic driving mechanism of the winds, whether by pressure or by momentum, and basic parameters like the mass loading factor are still unknown (e.g. Mac Low et al. 1989; Springel & Hernquist 2003; Murray et al. 2005; Oppenheimer & Davé 2008; Dalla Vecchia & Schaye 2012; Creasey et al. 2013). A further complication is that some winds may be driven by Active Galactic Nuclei (AGN). As a consequence, even when models predict a wind will be present, it is unclear how far the wind will travel, how much mass it carries, and even whether it will escape the galaxy into the intergalactic medium (IGM) or fall back onto the galaxy.

In contrast, numerical simulations have been very successful at predicting the properties of the lower density, largely quiescent intergalactic gas probed by the Lyα forest to high accuracy (Meiksin 2009). Despite lacking sub-grid implementations for winds, these models can nevertheless prove useful as a tool for interpreting and calibrating the absorption signatures of the gas around galaxies. To do so, however, it is necessary to establish how accurately the observable properties of the IGM may be predicted in these models, and to determine at which scales commonly used IGM simulation methodologies are no longer sufficient to model complex gaseous halo environments.

The purpose of this paper is to describe in detail the capacity and limitations of simulations specifically designed for modelling the IGM when applied to the extended gaseous environment of galaxies. This work will focus on moderate redshift galaxies in the range $2 < z < 3$ in particular, for which the surrounding gas has been probed by H I absorption line studies along lines of sight to background quasars, as in the Very Large Telescope Lyman-break galaxy redshift survey (Crighton et al. 2011) and the Keck Baryonic Structure Survey (Rudie et al. 2012). The latter authors in particular divide the gaseous environment of galaxies into three zones: a circumgalactic zone within 300 kpc (proper) of the galaxy, which approaches the turn-around radius of the galaxy haloes; an intermediate zone between 300 kpc and 2 Mpc (proper), and the ambient IGM at larger distances. The most massive haloes may also be useful for modelling the environments of quasar hosts, which show evidence for large amounts of cool gas (Hennawi et al. 2006; Prochaska et al. 2013). In this work we shall demonstrate that IGM simulations are able to converge on the physical properties of the gas outside the circumgalactic zone, specifically beyond the turn-around radii of the gas accretion onto the haloes, but require a detailed star formation prescription to model accurately the gas within. Any disagreement between the simulation predictions of H I properties and those measured beyond the turn-around radius would suggest winds influence gas outside the circumgalactic zone. We are examining this topic in a companion paper.

In order to demonstrate this, the two key factors we investigate in the IGM simulations are the uncertainty in the simulated halo masses associated with the observed galaxies, and the numerical agreement of the physical properties of the gas as computed by differing simulation methodologies. We use two widely used gravity-hydrodynamics codes for this purpose: `GADGET-3`, an updated version of the publicly available code `GADGET-2` (last described by Springel 2005), and `Enzo` (Bryan et al. 2014). In the first half of this paper we investigate the selection of dark matter haloes. No single halo-finding algorithm of the many in the literature is overall better than the rest; at some level the identification of haloes, and in particular the masses assigned to them, depend on arbitrary choices of technique. The issues involved have received wide attention in the literature for low redshift haloes (e.g. White 2002; Lukić et al. 2009; Bhattacharya et al. 2011; Onions et al. 2012; Knebe et al. 2013; Watson et al. 2013; Klypin et al. 2013; Velliscig et al. 2014), but less so for the redshifts of interest here, at $2 < z < 3$ (Reed et al. 2007; Tinker et al. 2008; Watson et al. 2013). We adopt three different methods and assess the differences in the properties of the haloes identified. In the second half of the paper, we compare the properties of the gas surrounding the haloes as computed by `GADGET-3` and `Enzo`.

All results are presented for a flat ΛCDM universe with the cosmological parameters $\Omega_m = 0.28$, $\Omega_b h^2 = 0.0225$ and $h = H_0/100$ km s^{-1} $= 0.70$, representing the total mass density, baryon density and Hubble constant, respectively. The intial matter power spectrum in the simulations has a spectral index $n = 0.96$, and is normalized to $\sigma_{8h^{-1}} = 0.82$, consistent with the 9-year *Wilkinson Microwave Anisotropy Probe* (*WMAP*) data (Hinshaw et al. 2013).

This paper is organised as follows. In the next section we describe the cosmological simulations used in this work. The halo catalogues constructed from these results are discussed in section 3, and the properties of the gaseous environments of the haloes are presented in section 4. Readers interested primarily in the comparison of the properties of gas around galaxy haloes in the simulations may skip directly to section 4. Our conclusions are summarised in section 5. A short appendix contains technical details on the convergence requirements and appropriate parameter choices when identifying dark matter haloes in the simulations.

2 NUMERICAL SIMULATIONS

2.1 Cosmological hydrodynamics codes

We use two widely used gravity-hydrodynamics codes in this analysis, one particle based and the other grid based. The

Table 1. Summary of the simulations performed in this work. The columns, from left to right, list the simulation name, the box size in comoving Mpc, the number of resolution elements in the simulation, the code used for the run, the star formation prescription and whether or not the model includes supernovae driven winds.

Name	Box size [Mpc]	Resolution elements	Method	Star formation	Winds
G30qLyα	30	2×512^3	GADGET-3	qLyα	N
G30sfnw	30	2×512^3	GADGET-3	SH03	N
G30sfw	30	2×512^3	GADGET-3	SH03	Y
E30_512	30	512^3	Enzo-2	none	N
E60_1024	60	1024^3	Enzo-2	none	N

particle based code GADGET-3, which is an updated version of the publicly available code GADGET-2 (Springel 2005), uses Smoothed Particle Hydrodynamics (SPH) to solve the fluid equations and a particle-based tree algorithm for gravity. By contrast, Enzo (Bryan et al. 2014) solves the fluid equations, including the gravity of the baryons, on a mesh, and the dark matter gravitational forces on the top level grid using a hybrid particle-mesh (PM) scheme. An extension of the method is to adapt the mesh resolution as necessary using adaptive mesh refinement. Tests show the success in resolving dark matter haloes below the top grid is sensitive to the means of triggering the refinements (O'Shea et al. 2005; Heitmann et al. 2008). We consider only unigrid (top level grid) simulations here, in keeping with the typical approach used for IGM analyses.

The numerical simulations were performed in boxes of size 30 Mpc (comoving) on a side using GADGET-3 and Enzo, v.2.1.1. As we focus on moderate redshift haloes, the runs were performed down to $z = 2$ only. The GADGET-3 simulations were run with 512^3 gas particles and 512^3 cold dark matter particles. The Enzo simulation was run with a top-level only grid of 512^3 mesh zones and 512^3 cold dark matter particles. The dark matter particle mass in these simulations is $m_c = 6.4 \times 10^6$ M$_\odot$, and the gas particle mass (or mean gas mass per grid zone) is $m_g = 1.3 \times 10^6$ M$_\odot$. These simulation parameters ensure good convergence on the statistics of the Lyα forest at $z \sim 2-3$ (Meiksin & White 2004; Bolton et al. 2005). As a test of convergence on the properties of the gas surrounding the haloes with box size, we also perform a second Enzo simulation in a 60 Mpc box with 1024^3 mesh zones and 1024^3 cold dark matter particles. We note the standard initial conditions generation routines differ between GADGET-3 and Enzo. We stress we have not sought to generate identical initial conditions for the two codes, but rather to examine differences between the overall code methodologies. In this sense we are not performing head-to-head code comparisons, but rather seeking the regime of agreement between two different generic IGM simulations using two widely used codes, examining in particular the gaseous environments of galactic mass haloes as computed by the simulations.

Both the Enzo and GADGET-3 computations used identical background photoionization histories and atomic rates for the heating and cooling, as discussed in Tittley & Meiksin (2007), except for adopting the HI electron excitation and collisional cooling rate of Scholz & Walters (1991). We use the photoionization and photoheating rates of Haardt & Madau (2012), which include contributions from both galaxies and quasars. The HeII heating rate was modified to reproduce the IGM temperature evolution of Becker et al. (2011) for $\gamma = 1.3$. The UV background is switched on at $z = 15$ and is applied in the optically thin limit. The codes were also modified to solve the non-equilibrium ionization rate equations.

Any computation of the IGM also requires a means of avoiding the high computational expense incurred by following rapidly cooling gas. Our focus in this study is on gas outside the galaxy haloes, within which the bulk of this cooling occurs. Nevertheless, the treatment of rapidly cooling gas will impact on the baryonic material throughout the vicinity of a halo. We therefore investigate the effects of different means of treating rapidly cooling gas on the simulation results in some detail. This enables us to establish the region around galaxies over which the means of treating unresolved rapidly cooling gas no longer affects predictions for the intergalactic gas, allowing reliable predictions to be made for comparison with observations.

The Enzo simulations bypass the problem of rapidly cooling gas by simply not spatially resolving regions that would produce rapid gas cooling. This is possible because the Jeans length of the IGM well exceeds the scales of rapid gas cooling in collapsed haloes. Because of its Lagrangian nature, however, GADGET-3 will inevitably track regions of high gas density and rapid cooling, so that some means of gas removal is necessary. We implement gas removal using two methods. The first is a simplified prescription, 'quick Lyα' (labelled G30qLyα below), which converts all gas particles with an overdensity $\Delta > 1000$ and gas temperature $T < 10^5$ K into collisionless particles (categorized as 'star' particles in the code), significantly speeding up the computation (Viel et al. 2004). We emphasize that this prescription is a computational trick and is not meant to represent actual star formation. A second method (G30sfnw) implements the multi-phase star formation prescription of Springel & Hernquist (2003). Although designed to include winds, we turn off the wind option to compare with the Enzo results. Lastly, we also perform a simulation (G30sfw) using the GADGET-3 supernovae driven wind model of Springel & Hernquist (2003), as an exploration of the impact a wind may have on the properties of the gas surrounding the haloes compared with the non-wind case. This model assumes a wind velocity of $484\,\mathrm{km\,s^{-1}}$, where each galaxy has a mass outflow rate twice its star formation rate, and the energy of the wind is equal to the energy released by supernovae. The simulations are summarised in Table 1.

2.2 Halo finding

Central to any statistical predictions of the properties of galaxies is the selection of simulated haloes meant to represent them. Various statistics are available to match haloes in a simulation volume to observed galaxies. The most straightforward is abundance matching. This involves simply matching simulated haloes to observed galaxies according to the rank order of the simulated halo masses and an observed extensive property of a galaxy, such as total luminosity or velocity dispersion. Another method compares the clustering strengths of galaxies and simulated dark matter haloes. No method is perfect, however, as the definition of a halo must contain some element of arbitrariness. Allowing for feedback in the form of radiation and galactic winds further complicates any matching procedure. Which definition relates best to observed galaxies is a matter of contention which likely will not be resolved without a more complete theory of galaxy formation. Many aspects of these issues have been explored in the literature (e.g. Frenk et al. 1988; Kravtsov et al. 2004; Vale & Ostriker 2006; Moster et al. 2010; Behroozi et al. 2013; Sawala et al. 2014).

In this study we focus our discussion on dark matter haloes in the mass range $11 < \log_{10}(M/\,\mathrm{M}_\odot) < 12$, although we shall consider trends outside this range as well. Based on clustering strength and luminosity-limited number counts, Trainor & Steidel (2012) estimate the galaxies in the sample of Rakic et al. (2012) from the Keck Baryonic Structure Survey occupy haloes with a minimum total mass (dark matter and baryons) of $\log_{10}(M/\,\mathrm{M}_\odot) > 11.7\pm0.1$ and a median total mass of $\log_{10}(M/\,\mathrm{M}_\odot) = 11.9\pm0.1$. These halo masses are also consistent with those inferred from the amount of H I absorption arising from the circumgalactic gas of the galaxies (Rakic et al. 2013).

We use two different particle based methods to select the haloes in the simulations: Friends-of-Friends (FoF) (Press & Davis 1982; Einasto et al. 1984; Davis et al. 1985)[1] and HOP (Eisenstein & Hut 1998). We also introduce a new method that selects haloes based on the density field interpolated onto a grid. The FoF algorithm joins all particles within a given fixed distance of one another, usually set according to the mean distance between particles. A disadvantage of FoF is that it sometimes links together sets of particles that to the eye would be regarded as separate haloes joined by a bridge. The HOP algorithm is designed to overcome this difficulty, forming groups by jumping to particles in ever denser neighbourhoods until no denser neighbour may be found. The groups tend to be more isolated than found using the FoF algorithm, although an allowance is made to join separate clumps if bridged by regions above a given density threshold. The HOP algorithm shares with FoF the advantage of being scale-free, but relies on more parameters. In practice, however, it is the outer density threshold for inclusion in a group that is the primary parameter that defines the group catalog. For FoF, we adopt the standard linking length of 0.2 the mean inter-particle separation. For HOP, we take $\delta_{\rm outer} = 80$, which we find gives good agreement with the FoF halo numbers. The remaining parameters are set in accordance with the recommendations in the documentation accompanying the HOP source code.[2]

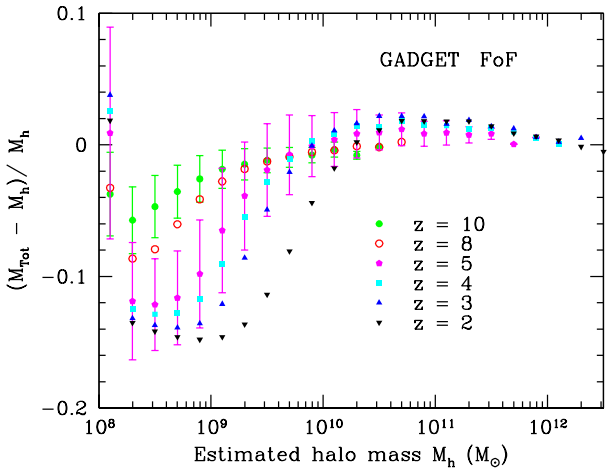

Figure 1. Difference between total halo mass $M_{\rm Tot}$ and rescaled dark matter halo mass M_h assuming the cosmic mean mass ratio of baryons to dark matter. Shown at $z = 2$, 3, 4, 5, 8 and 10 for haloes found using Friends-of-Friends in a `GADGET-3` run. The error bars indicate the 1σ spread in differences at $z = 5$ and 10.

The force softening scale for the `GADGET-3` runs is 1.4 kpc (comoving). Since `Enzo` uses the particle-mesh method, the force resolution is limited to two grid zones, or 118 kpc (comoving), adequate for resolving the Jeans length of the photoionized gas. The minimum virialized[3] halo mass achievable in the `Enzo` computation in a single cell is thus $18\pi^2(m_c + m_g) = 1.4 \times 10^9$ M$_\odot$. Allowing for a minimum of 27 cells to resolve a virialized halo in the gridded density field corresponds to a minimum mass of 3.7×10^{10} M$_\odot$. Much lower mass haloes are achievable in the `GADGET-3` run (and the `Enzo` run, if using adaptive mesh refinement) in principle, but not necessarily if the haloes are to avoid being under-resolved or over-relaxed in IGM simulations. Further details on this point may be found in the appendix.

[1] We use a publicly-available code at http://www-hpcc.astro.washington.edu/tools/fof.html .

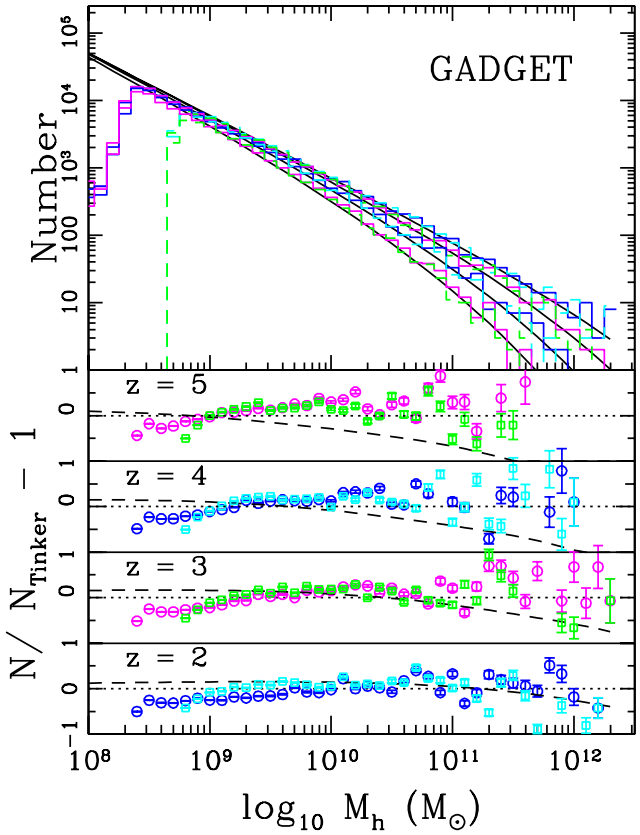

Figure 2. Halo mass distribution function at $z = 2$, 3, 4 and 5, for the G30qLyα `GADGET-3` simulation. *Upper panel:* Number of haloes found using FoF (solid; magenta and blue online, alternated for clarity) and HOP (dashed; green and cyan online, alternated for clarity), along with the expected number using the fit of Tinker et al. (2008) (black), with the sets of curves increasing at the high mass end from $z = 5$ to $z = 2$. The simulation results correspond to the total halo mass scaled from the dark matter component, assuming the cosmic mean mass ratio of baryons to dark matter. *Lower panels:* The fractional deviation of simulation halo counts from the model of Tinker et al. (2008), for the FoF haloes (circles) and HOP haloes (squares). The error bars are Poisson. The dashed lines show the expected counts using the fitting formula of Reed et al. (2007).

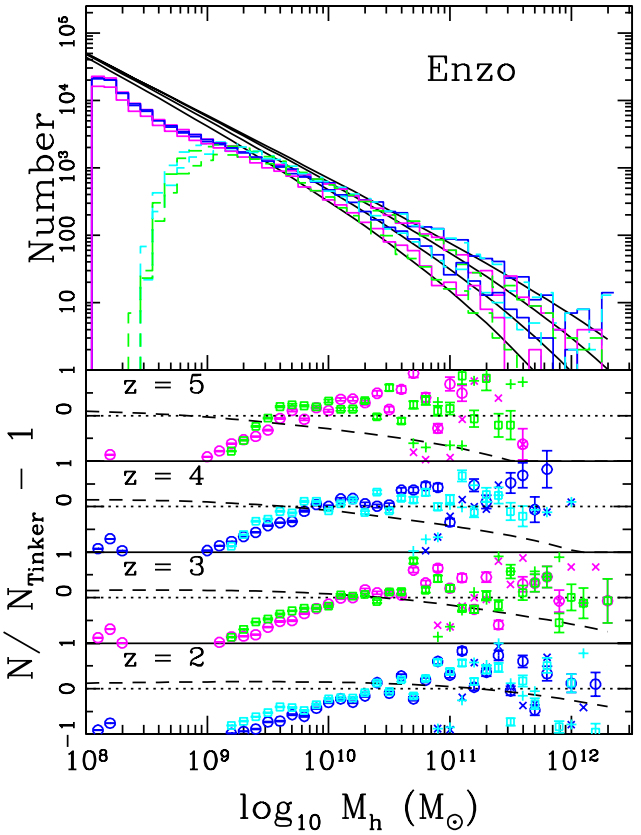

Figure 3. As for Fig. 2, except now showing the halo mass distribution function for the E30_512 `Enzo` run. Note the estimated minimal resolvable halo mass in this unigrid simulation is 4×10^{10} M$_\odot$. In the lower panels the halo masses for 'profiled' virialized haloes are shown by '+'s for FoF haloes, and by 'x's for HOP haloes (see text for further details).

3 HALO CATALOGUES

3.1 Baryon mass fraction in haloes

We now turn to describing the properties of the dark matter haloes in our simulations, before going on to discuss the gaseous environments of the haloes in section 4.

As most of the literature on haloes uses dark matter only simulations, the total halo mass (dark matter and baryons) is often scaled from the dark matter component assuming a uniform mass ratio of baryons to dark matter equal to the mean cosmic value, $\Omega_{\rm b}/(\Omega_{\rm m} - \Omega_{\rm b})$. We first test this assumption in Fig. 1 by applying FoF to the `GADGET-3` simulation G30qLyα for a range of redshifts. (Note the results are nearly identical for the G30sfnw simulation, which we do not show here.) The rescaled halo masses M_h are scaled from the dark matter assuming the cosmic baryon to dark matter mass ratio, and the actual halo masses $M_{\rm Tot}$, given by the combined mass of the dark matter, gas and star particles in the model, are found to agree closely over most of the halo mass range.

At the low mass end, however, discrepancies arise, with the actual mass systematically smaller than the rescaled mass, although with wide scatter. This difference arises primarily from heating by the UV background, increasing the thermal gas pressure and so impeding the inflow of the gas (e.g. Efstathiou 1992; Okamoto et al. 2008). The difference is small at $z = 10$ and 8, but by $z = 6$ the discrepancy exceeds 10 percent, with the range in discrepant masses systematically increasing with decreasing redshift. By $z = 2$,

[2] We take $N_{\rm dens} = 64$, $N_{\rm hop} = 16$, $N_{\rm merge} = 4$ with $\delta_{\rm outer} = \delta_{\rm saddle}/2.5 = \delta_{\rm peak}/3$, using the quantities defined in Eisenstein & Hut (1998).

[3] Haloes with central dark matter densities exceeding the virialization density will be referred to as 'virialized'; this is not meant to imply the haloes are necessarily in virial equilibrium. The virial mass M_V is the mass contained within the virial radius, defined here as the radius within which the average dark matter overdensity is $18\pi^2$ relative to the background dark matter density.

the discrepancy exceeds 10 percent for haloes less massive than 4×10^9 $M_\odot$, corresponding to a characteristic temperature of $T \simeq 50 \times 10^3$ K, comparable to the temperature of reionized intergalactic gas, including the enhanced heating rate as the UV metagalactic ionization background hardens, adiabatically compressed to virial densities. The effect of this redshift dependent baryonic physics suggests the dimensionless mass function shape is not universal to a precision better than 15 percent at the low halo mass end at these redshifts, even in the absence of supernovae feedback. With this mass discrepancy at the low mass end in mind, unless stated otherwise, halo masses in the remainder of this paper refer to values rescaled from the dark matter component assuming a uniform baryon to dark matter ratio at the cosmic mean value. As we focus primarily on halo masses in the mass range $11 < \log_{10}(M/\,\mathrm{M}_\odot) < 12$, this should be a reasonable approximation.

3.2 Halo mass function

The halo mass functions obtained by running FoF and HOP on the G30qLyα `GADGET-3` dark matter particles are shown in Fig 2. We compare the numbers of haloes found with the fitting formula of Tinker et al. (2008) for overdensity $\Delta = 200$ haloes[4] (solid black curves in upper panel), allowing for redshift dependent coefficients. Since this fitting formula was based on spherical overdensity haloes and the redshift dependence was limited to $0 < z < 2.5$, we also compare with the fitting formula of Reed et al. (2007) in the lower panels of the figure. This is based on haloes with masses $10^5 - 10^{12}\,h^{-1}$ $M_\odot$, identified over the redshift interval $0 < z < 30$ using FoF with a linking length of $b = 0.2$. The expected counts were generated using the `genmf` fitting formula code provided by Reed et al. (2007), adjusted to our cosmological parameters. Since we search for haloes using only the dark matter component, as noted earlier the total mass of the haloes is found by allowing for a baryon component at the cosmic mean ratio of baryons to dark matter. This matches the halo mass definitions of Tinker et al. (2008) and Reed et al. (2007).

The FoF halo mass distribution in Fig 2 agrees very closely with the fitting formula of Tinker et al. (2008), within the scatter, for halo masses $M > 2 \times 10^9$ $M_\odot$. The scatter sometimes exceeds the Poisson errors, based on the number of haloes found in a mass bin, but excess scatter is expected from large-scale structure, especially for the rarer haloes. At $z = 4$ and 5, the halo numbers continue to agree well with the Tinker et al. (2008) fitting formula, but deviate from the Reed fitting formula, which differs from the number of haloes we obtain by as much as ~ 50 percent at the high mass end, suggesting the fitting formula coefficients may not extend well to the different cosmological and power spectrum parameters we used, which more closely agree with those of simulations included in the Tinker et al. (2008) analysis.

[4] The halo mass is defined as the mass contained within a spherical surface centred on the halo and having an average internal overdensity 200 times the cosmic mean density. The halo masses using this definition well match those using FoF with $b = 0.2$ (Cole & Lacey 1996; Tinker et al. 2008).

The halo mass function for the HOP haloes is remarkably similar to the FoF halo mass function, within the scatter. There is a ~ 20 percent excess for $10^9 < M < 10^{10}$ $M_\odot$ at $z = 2$, bringing the numbers more closely in line with the Tinker et al. (2008) halo mass function. None the less, the differences in the counts suggests the algorithms are not always identifying the halo masses consistently. We return to this point below.

The halo mass functions from the E30_512 `Enzo` simulation, shown in Fig 3, also generally agree with the Tinker et al. (2008) mass function for haloes with $M > 2 \times 10^{10}$ $M_\odot$ for $z = 2$ and 3, although with considerable scatter. This mass threshold is comparable to the minimum mass for achieving a virialization density in 15 contiguous cells. The agreement extends down to 4×10^9 $M_\odot$ at $z = 5$. The mass functions found from the FoF and HOP algorithms generally agree, but vary at the ~ 20 percent level for halo masses below 10^{10} $M_\odot$. The more conservative halo resolution requirement of 27 contiguous mesh zones requires a minimum virialized halo mass of $M > 3.7 \times 10^{10}$ $M_\odot$, and we take this to be representative of the resolvable halo mass in the simulation.

Finally, we also 'profile' the haloes in the E30_512 `Enzo` simulation by first constructing spherical density profiles centred on the densest dark matter point in a halo, and then computing the virial mass of the halo by scaling from the dark matter mass to account for the baryonic component. The profiled results for virialized haloes are shown as 'x's for the FoF haloes, and '+'s for the HOP haloes in the lower panels of Fig. 3. The number of virialized haloes falls off abruptly below 10^{11} $M_\odot$ relative to the Tinker et al. (2008) mass function. As for the `GADGET-3` haloes, the numbers between the FoF and HOP haloes do not precisely match.

3.3 Minimum halo mass consistently identified by FoF and HOP

The principal source of the discrepancy between the halo mass distributions produced by different halo finding algorithms for well resolved haloes is generally not that different haloes are identified (although this may occur in unusually complex regions of massive mergers). Instead, different algorithms will typically assign different masses to the same haloes (e.g. Cohn & White 2008). However, provided these algorithms agree on the halo centres about which any subsequent radial density profiles are constructed, rank ordering the haloes by their estimated virial mass should provide a stable basis for comparing with observed galaxies; this approach will be largely independent of the means used for identifying the haloes. In this sub-section, we therefore examine the minimum halo mass for which FoF and HOP, as applied to the `Enzo` data, produce identical virial masses. Note that since `GADGET-3` resolves halo density profiles to smaller scales than `Enzo`, the corresponding minimum halo mass of `GADGET-3` haloes will be smaller. We therefore confine our discussion of the minimum consistently identified halo mass to the `Enzo` data only.

We first compare the masses of individual haloes identified by both FoF and HOP by one-to-one matching HOP and FoF haloes identified in the E30_512 `Enzo` simulation. We achieve this by searching for the nearest HOP halo within the virial radius of a FoF halo. A comparison between the

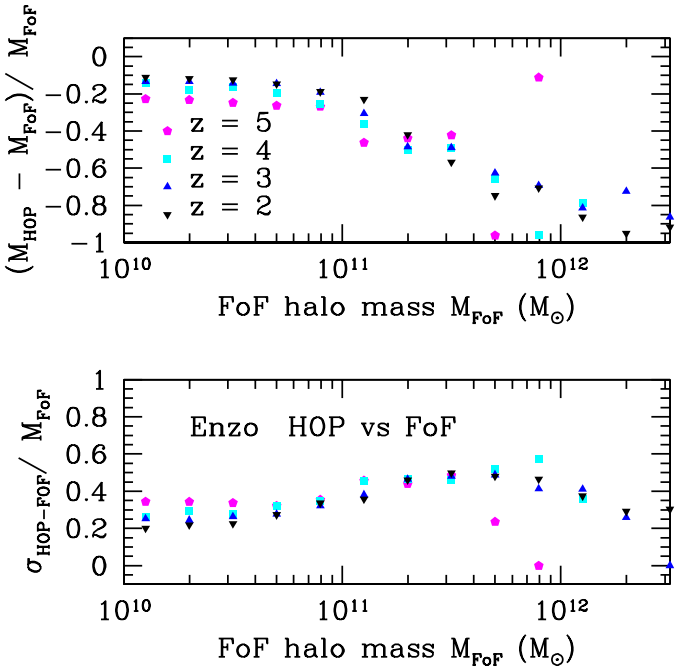

Figure 4. The difference between the FoF and HOP halo masses from the E30_512 `Enzo` run as a function of FoF halo mass. The halo match is based on finding the HOP halo which lies within the virial radius of a given FoF halo with the most similar mass. The comparison is shown at $z = 2$, 3, 4 and 5. *Upper panel:* Mean difference in the halo masses. *Lower panel:* The standard deviation in the difference between halo masses.

halo masses is shown in Fig. 4. The HOP halo mass generally agrees well (to within around 20 per cent) with the FoF halo mass below 10^{11} $M_\odot$. At higher masses, however, the HOP halo masses are increasingly low compared with the corresponding FoF mass, consistent with HOP's breaking up chains of particles that FoF links together into the same halo. This shows that, while the halo finders identify the same peaks, they associate somewhat different particles to the resulting haloes. As a consequence, the FoF and HOP haloes do not maintain the same rank ordering by mass, with a spread in mass difference of around 20–60 percent, as shown in the lower panel of Fig. 4. In the absence of a more precise definition of halo mass, this partially undermines the use of rank ordering when associating simulated haloes with observed galaxy properties.

The virial mass (which we obtain by profiling the haloes in the manner described previously) offers a much better definition for this purpose, since the rank ordering is preserved by the different halo finders above a minimum halo mass. To demonstrate the stability of the virialized halo masses against the choice of halo finder for sufficiently massive haloes, we one-to-one match virialized haloes found by FoF and HOP. At $z = 3$, nearly one-third of the virialized FoF haloes have no matching virialized HOP halo located within the virial radius of the FoF halo. Conversely, nearly one-quarter of virialized HOP haloes have no matching virialized FoF halo. Almost all the unmatched haloes have masses below 2×10^{11} $M_\odot$. For the remaining majority of virialized haloes, the total halo masses within the virial radius computed from the density profiles centred on the density peak found by either halo finder agree almost exactly. Thus the virial masses of essentially all virialized haloes with masses above 2×10^{11} $M_\odot$ agree, whether identified using FoF or HOP. Should future surveys extend measurements of circumgalactic gas to smaller halo masses, a grid code like `Enzo` would then require higher spatial resolution than we have used, either using a finer top-grid or an adaptive mesh, going beyond the standard requirements for an IGM simulation.

3.4 Grid-based halo finder

An alternative approach to particle based halo finders is to identify haloes on the dark matter density grid. For large simulations, this has the advantage of requiring far less data to be saved, particularly for a hydrodynamical grid code. Moreover, since the gravitational force is computed on a grid in mesh codes, haloes found from the gridded density field will more faithfully reflect the resulting mass concentrations.

Motivated by these considerations, we have developed a gridded density field halo finder (GHF) similar to the search for spherical overdensities in N-body data (Warren et al. 1992; Lacey & Cole 1994), although our method is based on the local density rather than a mean internal density, and so tracks the filamentary structure of overdense regions. Specifically, the method grows haloes by building them up in concentric shells about density peaks, with the following procedure: 1. Identify all the density peaks of the gridded density field, and rank order them from highest to lowest. 2. Working down the list from the highest peak, search among the next nearest layer of mesh cells for those with densities above a given threshold overdensity $\Delta_{\rm th}$. 3. If a cell incorporated on the list appears on the list of density peak cells, remove it from the list of peaks. (It is assumed incorporated into the halo with a higher density peak.) 4. If the fraction of cells more overdense than $\Delta_{\rm th}$ exceeds a given value $p_{\rm th}$, repeat step 2 extending to the next layer; otherwise cease growing the halo and go to the next density peak on the list. Choosing $\Delta_{\rm th} = 178$ will grow approximately spherical virialized haloes.

The resulting halo counts are shown in Fig. 5 for the G30qLyα `GADGET-3` simulation (upper panel) and E30_512 and E60_1024 `Enzo` simulations (lower panel). The `GADGET-3` dark matter particles are gridded onto meshes with 256^3, 512^3 and 1024^3 cells. The halo counts lie 30–50 percent lower than predicted by the Tinker et al. (2008) halo mass function, with the deficit increasing towards lower mass haloes. The agreement improves at the low mass end with increasing mesh resolution, but otherwise the counts are largely insensitive to the regridding resolution. Haloes on a 512^3 (256^3) grid are recovered to 30–50 percent down to 2×10^{10} $M_\odot$ (2×10^{11} $M_\odot$).

The number counts of haloes found from the gridded

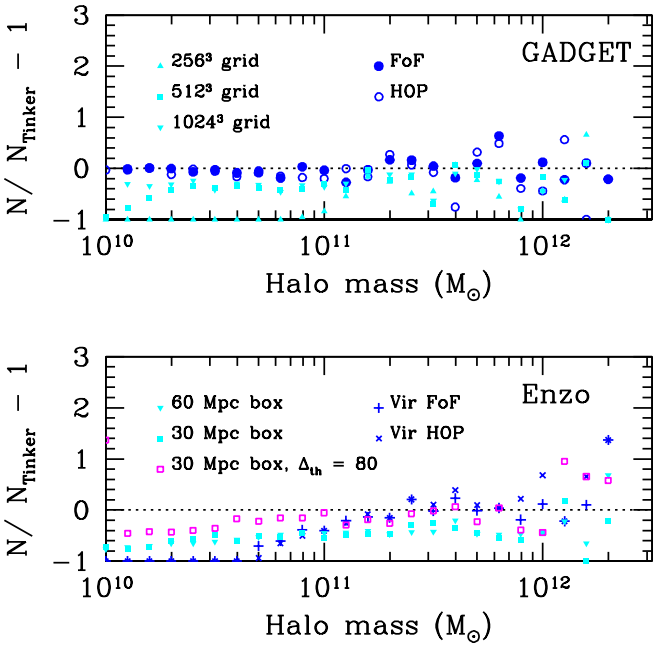

Figure 5. Differential number counts of haloes at $z = 3$ identified using a gridded density field halo finder (GHF) based on the dark matter density field with a threshold density set at the virialization density, relative to the Tinker et al. (2008) fitting function. *Upper panel:* Results for the G30qLyα `GADGET-3` density field gridded onto meshes with 256^3 (cyan triangles), 512^3 (cyan squares) and 1024^3 (cyan inverted triangles) cells. For comparison, the counts of haloes found using FoF (blue filled circles) and HOP (blue open circles) finders are also displayed. *Lower panel:* Results for the haloes found from the dark matter density field for two `Enzo` simulations of fixed resolution, but with comoving box sizes of 30 Mpc (cyan squares) and 60 Mpc (cyan inverted triangles). Also shown are the results for haloes found above a threshold overdensity of 80 (cf. $18\pi^2$) in the 30 Mpc box (magenta open squares). For comparison, the counts of virialized haloes found using FoF (blue '+'s) and HOP (blue 'x's) are also shown.

dark matter density field in the `Enzo` 512^3 30 Mpc volume simulation likewise lie systematically low compared with Tinker et al. (2008), by about 30–60 percent. Using the density field from a second `Enzo` simulation in a 60 Mpc box with the same grid resolution as for the 30 Mpc box simulation, and setting $\Delta_{\rm th} = 178$, provides comparable halo numbers to the 30 Mpc box, as shown in Fig. 5. The halo numbers are reasonably well converged, so box size does not account for the differences. The discrepancy may be attributed in part to the difference in the extents of the haloes. Lowering the overdensity threshold from $\Delta_{\rm th} = 178$ to 80 provides much better agreement with Tinker et al. (2008). As shown in the appendix, lowering this threshold increases individual halo masses, putting them into better agreement with the masses of the matching FoF haloes.

3.5 Observational prediction uncertainties due to uncertainty in halo mass assignments

Finally, we note that the sensitivity of halo mass rankings to the halo finding algorithm introduces uncertainty into the assignment of halo masses to observed galaxies if abundance matching is used as a basis (see e.g. Sawala et al. 2014, for several references to the literature on abundance matching). As we have discussed here, one way to approach the problem is to use only haloes well resolved within their virial radii, and then rank them by some fixed criterion like virial mass. Since different halo finders mostly identify the same structures when well resolved, the masses about the halo centres will generally agree. For this reason we restrict our analysis in the next section to haloes with $11 < \log_{10}(M/\,{\rm M}_\odot) < 12$. How successful this approach is at matching observed galaxies, however, remains an open question.

There are also a large number of lower mass haloes which do not have well resolved virial cores in our simulations that may still be useful for statistical analyses. The uncertainty in the masses of these haloes will give rise to an uncertainty in any predicted properties of observed galaxies and their environments. An approximate means of estimating the impact of the uncertainty in halo mass on the dispersion in a predicted property is to average it over a Gaussian distribution, allowing that any given halo finding algorithm may err in the assignment of halo mass M_h with a standard deviation $\sigma(M_h) = \beta M_h$. We have found typical values of $\beta = 0.2 - 0.4$ in our analysis above (e.g., Fig. 4). For a property that may be approximated as a power law in mass, $f(M_h) \sim M_h^\alpha$, it is then straightforward to show that in the limit $|\alpha(\alpha-1)|\beta \ll 1$, the mean is only quadratically biased, $\langle f\rangle/\langle f\rangle_{\beta=0} - 1 \simeq (1/2)\alpha(\alpha-1)\beta^2$, while the relative standard deviation is $\sigma_f/\langle f\rangle \simeq |\alpha\beta|$. As an example, the estimated velocity dispersion of a halo, $v_{\rm rms} \sim (GM_h/r_V)^{1/2} \sim M_h^{1/3}$, will be biased low by 1 percent, with a relative spread of 10 percent, for $\beta = 0.3$. Since the actual halo mass probability distribution may have a broad tail, this approach may conservatively be regarded as providing a lower limit on the uncertainty.

4 INTERGALACTIC MEDIUM PROPERTIES AROUND HALOES

4.1 Halo peculiar velocities

In this section, we now turn to analysing the properties of the gas around galaxy haloes with total masses $11 < \log_{10}(M/\,{\rm M}_\odot) < 12$, corresponding to the haloes of galaxies with measured H I absorption in their environments. These haloes also tend to be relatively isolated, permitting clearly delineated radial profiles of the gas propertires to be constructed.

We first examine the convergence of the gas peculiar velocity field. Because the peculiar velocity power spectrum peaks on scales in excess of 100 Mpc (comoving), this is not expected to fully converge in our 30-60 Mpc boxes on large

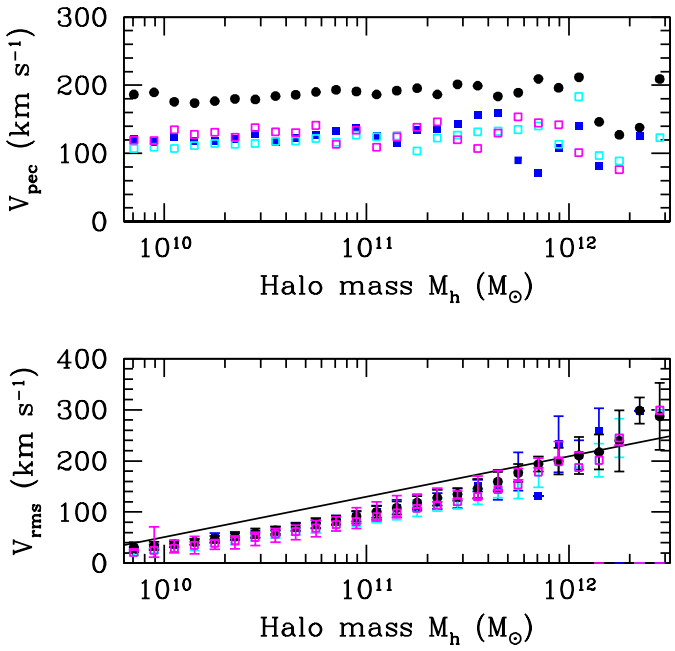

Figure 6. Convergence of the halo peculiar velocities (top panel) and internal velocity dispersion of the gas (lower panel) for the `Enzo` simulations E30_512 (filled squares; blue) and E60_1024 (filled circles; black) at $z = 3$, as a function of halo mass. Also shown are the values for halo masses using a lower overdensity threshold of 80 in E30_512 (open squares; cyan). The results for haloes in the `GADGET-3` simulation G30sfnw (open squares; magenta) agree well with the results for the corresponding `Enzo` haloes. The solid line in the lower panel shows $v_{\rm circ}/2^{1/2}$, where $v_{\rm circ}$ is the circular velocity at the virial radius.

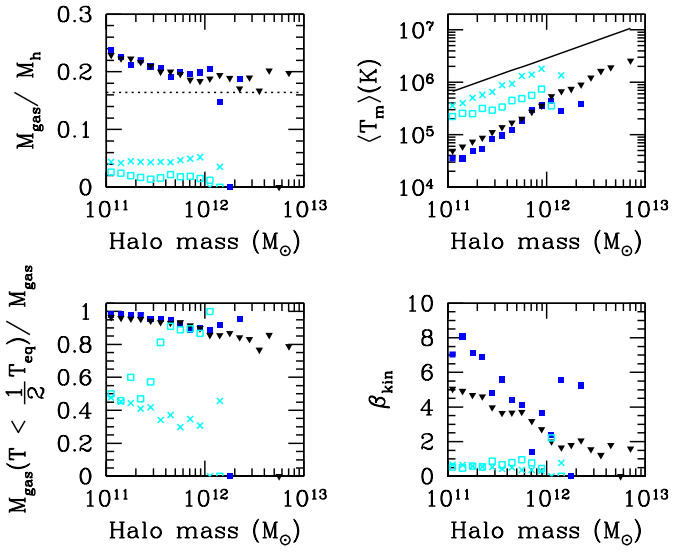

Figure 7. Thermal and kinetic properties of the gas within the virial radius of haloes at $z = 3$. Results shown for the `Enzo` simulations E30_512 (blue filled squares) and E60_1024 (black filled inverted triangles). Also shown are results for the `GADGET-3` simulation G30sfnw with the gas interpolated onto a 512^3 cell grid (cyan open squares) and the `GADGET-3` wind simulation G30sfw (cyan crosses). Clockwise from the top left, the panels show the gas mass fraction (the dotted line displays the cosmic mean), the mean mass-weighted temperature, the ratio $\beta_{\rm kin}$ of the gas kinetic to thermal energies and the gas mass fraction with a temperature less than half the halo equipartition temperature. The solid line in the upper right panel is the predicted post-shock temperature as a function of halo mass.

scales. In Sec. 4.3 below we address the radial scale over which the peculiar velocity field of a halo converges.

The convergence of the halo peculiar velocity and internal velocity dispersion $v_{\rm rms}$ of the gas at $z = 3$ is shown in Fig 6 for GHF haloes with $\Delta_{\rm th} > 178$ for the E30_512 and E60_1024 `Enzo` and the G30sfnw `GADGET-3` simulations. The `GADGET-3` data are binned onto a 512^3 mesh to match the `Enzo` spatial resolution. Doubling the box size of the `Enzo` simulation from 30 to 60 Mpc (comoving) nearly doubles the peculiar velocities of the haloes, showing they have not converged. The halo peculiar velocity is independent of halo mass, showing the haloes behave as test particles in large scale flows. The internal velocity dispersion of the `Enzo` haloes, in contrast, is well converged with box size. The values for the `GADGET-3` haloes agree with those for the `Enzo` haloes for the corresponding mass bin, as expected if both codes are producing the same structures for a given halo mass. Comparison with the halo circular velocity at the virial radius, $v_{\rm circ} = (GM_h/r_v)^{1/2}$, shows that the gas is dynamically cool, with $v_{\rm rms} \lesssim v_{\rm circ}/2^{1/2}$.

4.2 Circumgalactic gas properties

The thermal and kinetic properties of the gas within the virial radius of haloes at $z = 3$ are shown in Fig. 7. The results are averages over all haloes in mass bins of width $\Delta \log_{10} M_h = 0.1$. The values shown for the `Enzo` runs (blue and black symbols) test the convergence of the halo internal gas properties with box size for 30 and 60 Mpc (comoving) boxes. Results for the corresponding `GADGET-3` runs with star formation both without a wind (cyan squares) and with a wind (cyan crosses) in the 30 Mpc box, gridded onto a 512^3 mesh to match the `Enzo` 30 Mpc box, are shown for comparison.

The gas mass fraction for the `Enzo` haloes is well converged with box size. For $M_h > 10^{12}$ M$_\odot$, the gas mass fraction lies just above the cosmic mean value ($\Omega_b/\Omega_m \simeq 0.164$), increasing towards lower masses, until 50 percent over-abundant for $M_h = 10^{11}$ M$_\odot$ haloes. By contrast, star

formation in the GADGET-3 simulation G30sfnw leaves behind only a small fraction of the baryons within the virial radius in the form of gas, the remainder having been converted into stars. Adding wind feedback in the G30sfw simulation balances the gas density at somewhat higher values.

The mean mass-weighted temperature of the gas is defined by $(3/2)k\langle T_m\rangle/\mu m_{\rm H} = E_{\rm th}/M_{\rm gas}$, where $E_{\rm th}$ is the total thermal energy of the gas mass $M_{\rm gas}$ within the virial radius, μ is the mean molecular weight for a fully ionized hydrogen and helium gas and $m_{\rm H}$ is the mass of a proton. The temperature is well converged for the Enzo simulations, as shown in Fig. 7, although the convergence worsens for the lower mass haloes. The temperature of the more rarefied gas in the GADGET-3 simulations is considerably higher. For an adiabatic shock, the post-shock temperature of a halo of mass M_h collapsing at redshift z is $T_{\rm shock} \simeq 72.1(1+z)(M_h/10^6\ {\rm M}_\odot)^{2/3}$ (Meiksin 2011). The temperature in the GADGET-3 non-wind simulation G30sfnw lies at about one-third this limit, suggesting radiative losses have been moderately effective in cooling the post-shock gas. Allowing for a wind in simulation G30sfw produces somewhat higher temperatures. By contrast, the gas in the Enzo simulations shows considerable cooling, but does not lead to runaway cooling on the resolution scale of the grid.

Almost all the gas in the Enzo haloes is colder than half the halo equipartion temperature $T_{\rm eq}$, defined by $(3/2)\langle k/\mu m_{\rm H}\rangle T_{\rm eq} = GM_h/r_v$. Nearly the same amounts are found for the GADGET-3 haloes in simulation G30sfnw with halo masses exceeding 4×10^{11} M$_\odot$. In lower mass haloes, cooling is less efficient, with only half the gas cooler than half the equipartition temperature. In the wind simulation G30sfw, the more massive haloes have a much smaller proportion of cool gas, with only one third to one half cooler than half the equipartition temperature.

The gas internal kinetic energy of a halo is defined by $E_K = (1/2)\int dV\,\rho_g(\mathbf{v}_{\rm pec}-\mathbf{v}_h)^2$, where ρ_g is the gas density, $\mathbf{v}_{\rm pec}$ is the gas peculiar velocity and $\mathbf{v}_h$ is the centre-of-mass peculiar velocity of the gas in the halo. The ratio $\beta_{\rm kin} = E_K/E_{\rm th}$ indicates the balance between the kinetic and thermal energies of the gas. For Enzo haloes with $M_h > 10^{12}$ M$_\odot$, the energies are nearly in equipartition, with the kinetic energy slightly larger. The ratio increases to factors of several towards the lower mass haloes. Comparison between the 30 and 60 Mpc boxes suggests $\beta_{\rm kin}$ is not yet well converged, with the value decreasing with increasing box size. For the GADGET-3 haloes, $0.5 < \beta_{\rm kin} \lesssim 1$, suggesting that the gas too rarefied to rapidly cool and make stars reaches equipartition between the kinetic and thermal energies.

The large differences between the Enzo and GADGET-3 circumgalactic gas properties demonstrate that the behaviour of the gas may not be reliably computed outwith a specific star formation model, even before feedback effects are included. If the star formation efficiency moreover depends on the internal gas kinematic properties, then accurate predictions for the properties of circumgalactic gas pose a severe computational challenge, requiring both high spatial resolution to follow rapidly cooling gas as well as a large simulation volume to produce accurate gas flow fields.

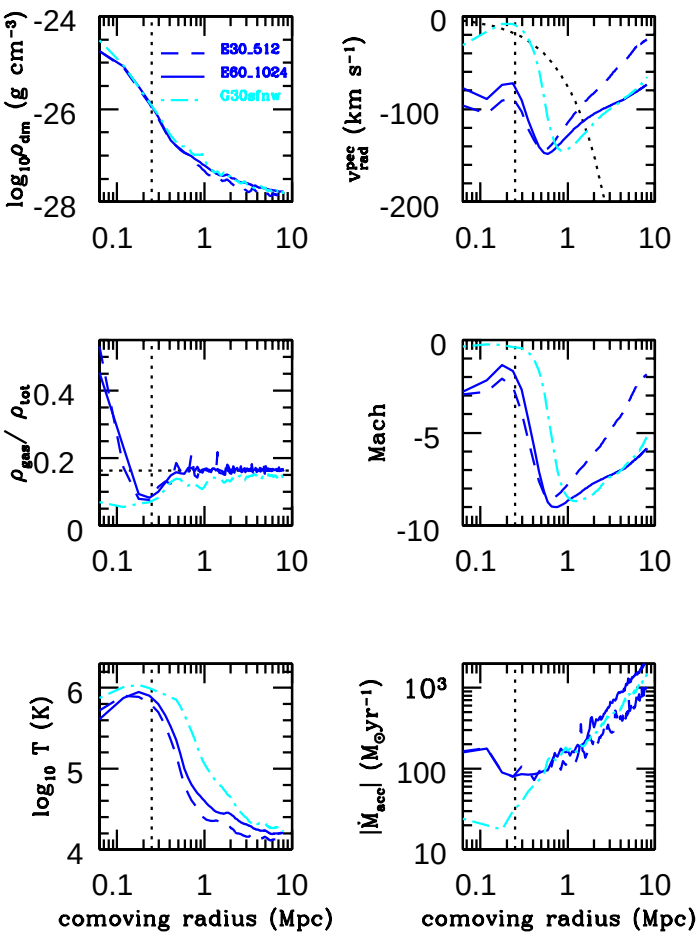

Figure 8. Mean radial profiles of halo properties at $z = 3$ with total masses of 4.5×10^{11} M$_\odot$, for GADGET-3 simulation G30sfnw (dot-dashed lines; cyan), and Enzo simulations E30_512 (dashed lines; blue) and E60_1024 (solid lines; blue). Clockwise from the upper left, the panels display: the dark matter density, the gas peculiar velocity, the Mach number, the mass accretion rate, gas temperature and the gas density. The vertical dotted lines in each panel show the virial radius of the haloes. The curved dotted line in the upper right panel shows the Hubble expansion (as negative velocity): the intersection with the peculiar velocity curve indicates the instantaneous turn-around radius of the gas in the haloes, located at $r_{t.a.} \simeq 6r_v$.

4.3 Radial profiles

Radial profiles of the dark matter density and gas properties for a representative halo mass of 4.5×10^{11} M$_\odot$ are shown in Fig. 8, for both the GADGET-3 and Enzo haloes in 30 Mpc boxes, as well as Enzo haloes in the 60 Mpc box. The profiles are averaged over all haloes within a mass bin of width $\Delta\log_{10} M = 0.1$.

A detailed comparison between E30_512 and E60_1024

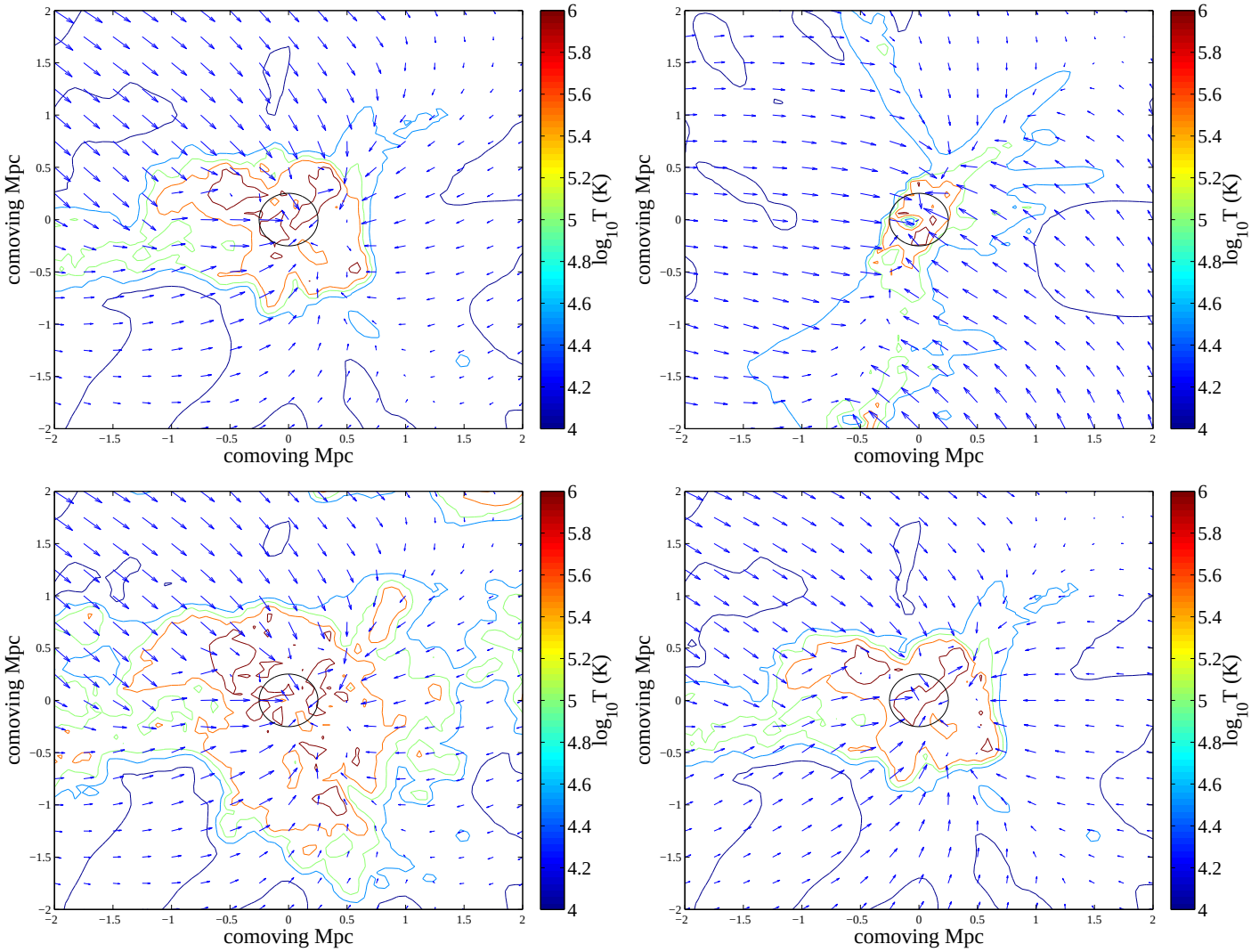

Figure 9. The effects of the prescription for the treatment of unresolved, rapidly cooling gas on the gaseous environment of haloes, illustrated for representative haloes at $z = 3$ with masses $\sim 5 \times 10^{11}$ $M_\odot$ from `GADGET-3` and `Enzo`. The boxes are 4 comoving Mpc on a side and centred on the haloes. Shown are slices of the gas temperature field and peculiar velocity flow relative to the halo centres-of-mass. The colour bars show $\log_{10} T$. An arrow of one axis tic unit in length corresponds to a velocity magnitude of 1000 km s^{-1}. The black circles indicate the virial radii of the haloes. The panels show haloes in simulations, clockwise from the top left, G30sfnw, E30_512, G30qLyα and G30sfw. A broad region of hot rarefied and kinematically quiescent gas develops around the `GADGET-3` haloes as a result of efficient removal of rapidly cooling gas, with enhanced energy input from a wind in simulation G30sfw. In the `Enzo` simulation, gas removal is suppressed by the limited spatial resolution, resulting in a more compact and kinematically active halo of multiphase gas.

shows agreement in the dark matter profiles (upper left panel) within twice the virial radius to 10 percent, and at 30 percent beyond in the secondary infall region. The difference may be partly due to low numbers since there are only 11 haloes in the mass bin. The dark matter profiles of haloes with somewhat lower masses (not shown) agree to 15 percent between the two box sizes. The `GADGET-3` mean dark matter profile agrees better with the larger box `Enzo` simulation. The agreement demonstrates that both `GADGET-3` and `Enzo` are reproducing similar dark matter structures as identified by halo mass, and that these structures are reasonably well converged with respect to simulation box size.

The `Enzo` simulations have well converged on the physical state of the intergalactic gas outside the turn-around radii of the haloes. For radial distances $r > 2$ Mpc (comoving), the gas density profiles agree to within 10 percent and the temperatures to better than 30 percent (middle and lower left panels). The peculiar inflow velocity and Mach number agree less well (upper and middle right panels), although we note somewhat smaller mass haloes show agreement over $2 < r < 4$ Mpc to within ~ 30 percent, but deviate at larger radii. The mass accretion rate (lower right panel), defined in terms of the radial peculiar velocity $v_{\rm rad}^{\rm pec}$ as $\dot{M}_{\rm acc} = 4\pi r^2 \rho_{\rm gas} v_{\rm rad}^{\rm pec}$, is noisier, and shows agreement only at the 50 percent level over $2 < r < 4$ Mpc. At larger radii, the mean inflow velocity departs substantially between the two box sizes, showing poor convergence. This reflects the non-convergence of the large-scale peculiar velocity field noted in section 4.1. We note that the instantaneous turn-around radius of the gas, where the gas breaks away from

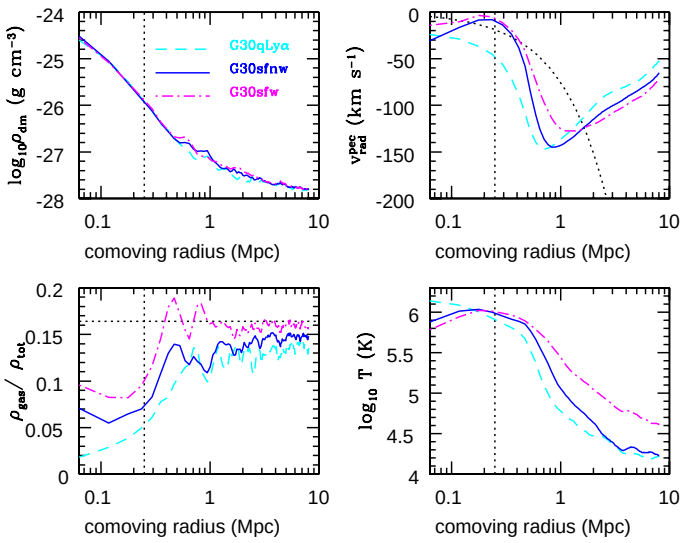

Figure 10. Mean radial profiles of halo properties for GADGET-3 haloes at $z = 3$ with total masses of 4.5×10^{11} $M_\odot$, for simulations G30sfnw (solid lines; blue), G30qLyα (dashed lines; cyan) and G30sfw (dot-dashed lines; magenta). Clockwise from the upper left, the panels display: the dark matter density, the gas peculiar velocity, gas temperature and the gas density. The vertical dotted lines in each panel show the virial radius of the haloes. The curved dotted line in the upper right panel shows the Hubble expansion (as negative velocity): the intersection with the peculiar velocity curve indicates the instantaneous turn-around radius of the gas in the haloes, located at $r_{t.a.} \simeq 6r_v$.

the Hubble expansion and begins flowing inward, is located at $r_{t.a.} \simeq 6r_v$ as shown in the top right panel of Fig. 8. This is close to the value $\sim 4r_v$ for the self-similar secondary infall of an adiabatic $\gamma = 5/3$ collisional gas onto a collapsed dark matter halo in an Einstein-de Sitter universe (as inferred from table 8 of Bertschinger 1985).

While the dark matter profiles agree between the GADGET-3 and Enzo haloes, the gas profiles within the circumgalactic region show large differences. The Springel & Hernquist (2003) star formation prescription in the GADGET-3 simulation has removed most of the baryons within the virial radius from the gas phase. A wide region of hot gas develops in the GADGET-3 haloes extending over ~ 3 virial radii, as illustrated in Fig. 9. By contrast, in the Enzo haloes the hot gas region is more compact, with the hot gas component confined to the inner 1–2 virial radii. A consequence is a lower Mach number for the accreting gas within the GADGET-3 haloes, and a more quiescent velocity field within and around the haloes. Dense pockets of cooling gas develop in the Enzo haloes, as illustrated in Fig. 9, resembling cold streams (Birnboim & Dekel 2003; Kereš et al. 2005). An extended warm stream entering from the left is visible in the GADGET-3 haloes.

Outside the turn-around radius, the GADGET-3 and Enzo results agree well. The baryon fraction in the GADGET-3 haloes is found not to converge to the cosmic mean value to better than 10 percent by a radial distance of 8 Mpc, as shown in Fig. 8, suggesting gas removal has been efficient in the surrounding smaller mass haloes. The GADGET-3 temperature agrees best with the larger box Enzo simulation, to within 30 percent beyond $r > 3$ Mpc. This may partly be an effect of the gas removal in the GADGET-3 simulation, leaving behind lower density but higher temperature gas. Achieving better agreement between Enzo and GADGET-3 simulations appears to require a specific model of star formation: the means of dealing with unresolved rapidly cooling gas has become a limiting factor in the predictive capacity of the simulations for intergalactic gas near the haloes.

A comparison of the radial profiles of the dark matter density and gas properties for 4.5×10^{11} $M_\odot$ haloes from the three GADGET-3 simulations is shown in Fig. 10. This directly compares the effect of different star formation prescriptions on the gas properties. The dark matter density profiles are essentially unaffected by the mode of gas removal or the presence of a wind within the virial radius, but changes of a few tens of percent appear in the secondary infall region beyond the virial radius. The gas density of the simulations without a wind lies below the cosmic value out to 8 Mpc, with the quick Lyα simulation removing gas most efficiently. Invoking a wind slows the infall velocity of the gas, but has not produced outflow[5] in terms of the peculiar velocity. The position of the outer turn-around radius of the gas remains unchanged. Less gas is removed from the central regions. A moderate amount of gas compression occurs beyond the virial radius, with the gas returning to the cosmic mean baryon density (shown by the horizontal dotted line) beyond the turn-around radius.

Lastly, we note that uncertainty in the simulated halo masses assigned to galaxies will introduce further uncertainty into the predicted properties of the intergalactic gas near the haloes. The magnitude of the uncertainty is illustrated in Fig. 11 for a GHF Enzo halo mass of $10^{11.55}$ $M_\odot$, showing the consequences of assigning gas properties corresponding to haloes with mass offsets of $\Delta \log_{10} M_h = \pm0.1$ and ±0.3. A halo offset of ±0.1 is representative of the differences in mass assigned to haloes by the different halo finding algorithms we used. The resulting neutral hydrogen density $n_{\rm HI}$ and temperature T differences are 10–20 percent at $r > 1.5$ Mpc. A mass offset of ±0.3 produces differences of 20–40 percent. Comparable relative differences are found for the total radial velocity except near the turn-around radius. The absolute radial velocity offsets range up to $20 - 30$ km s^{-1}. The relatively modest differences in the physical properties of the intergalactic gas near haloes (at scales above the turn-around radius) for a range of halo masses suggest good tolerance of the predictions to the larger uncertainties in the halo masses. The converse is that the local circumgalactic gas properties can provide only a crude estimate of the masses of the central haloes.

[5] Note also that in the Springel & Hernquist (2003) model, winds remain hydrodynamically decoupled from the gas until the gas density is less than 10 per cent the star formation threshold density, or if more than 50 Myr has elapsed since the wind particle is launched.

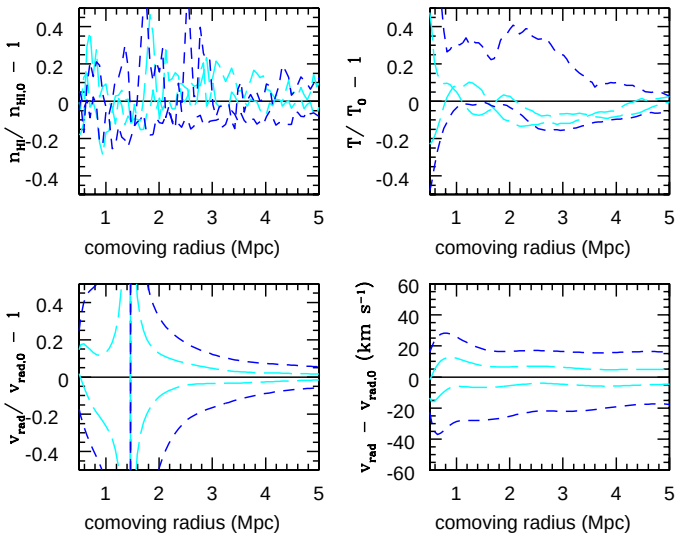

Figure 11. Percentage differences of halo mean radial profiles from $10^{11.55}$ $M_\odot$ **Enzo** haloes in 60 Mpc box, for haloes with mass offsets $\Delta \log_{10} M_h = \log_{10} M_h - 11.55 = \pm 0.1$ (cyan long-dashed lines) and ± 0.3 (blue short-dashed lines). Anti-clockwise from top right, the panels display relative differences in the gas temperature, the neutral hydrogen fraction and the radial velocity. The absolute velocity difference is shown in the lower right panel. The divergence in the relative velocity error corresponds to the instantaneous turn-around radius at $\gtrsim 1.4$ Mpc.

5 SUMMARY AND CONCLUSIONS

We investigate how well simulations designed to study the IGM reproduce the physical properties of the gas surrounding galaxy haloes, motivated by recent observations of the gaseous environments of redshift $z \sim$ 2–3 galaxies through H I absorption line measurements (Steidel et al. 2010; Crighton et al. 2011; Rudie et al. 2012; Prochaska et al. 2013). To do so, we perform comparisons of the dark matter and gaseous properties of moderate redshift haloes, with $2 < z < 5$, using two different numerical simulation codes, **GADGET-3** and **Enzo**. We have examined two separate issues, agreement in the halo masses and abundances, necessary for reliably selecting simulated haloes to represent observed galaxies, and agreement in the physical properties of the gas around the haloes. We summarise our results on these topics separately.

Our main results concerning halo selection are:

1. For halo masses exceeding 10^{10} $M_\odot$, rescaling the dark matter halo mass by the mean cosmic baryon to dark matter density ratio reproduces the total halo mass (comprised of dark matter and baryons) to a few percent accuracy. We find, however, that the rescaling over-estimates the true combined dark matter and baryon mass of haloes with masses below 10^{10} $M_\odot$ by as much as 15 percent, with the discrepancy increasing at decreasing redshifts. This difference is due to the partial loss of gas in the smaller mass haloes as a result of photoionization heating (e.g. Okamoto et al. 2008).

2. Reasonable agreement is obtained between the numbers of FoF and HOP haloes found in the **GADGET-3** simulation and the corresponding **Enzo** simulation. The halo mass functions agree with that of Tinker et al. (2008) to about 10–30 percent accuracy over the total halo mass range $10^9 < M_h < 10^{11}$ $M_\odot$ for the **GADGET-3** haloes and over $10^{10} < M_h < 10^{11}$ $M_\odot$ for the **Enzo** haloes, although the halo abundances evolve somewhat more slowly with redshift for $z > 2$ (beyond the redshift range considered by Tinker et al. 2008). There is substantial scatter, 30–50 percent differences from the fitting formula, at higher masses due to the low numbers of haloes and cosmic variance in our 30 Mpc (comoving) simulation boxes.

3. A one-to-one matching of FoF and HOP haloes in the **Enzo** 30 Mpc box simulation shows that the HOP halo masses are typically 20 percent smaller than the FoF halo masses for FoF halo mass below 10^{11} $M_\odot$, nearly independent of redshift. The discrepancy increases to as much as 80 percent low for 10^{12} $M_\odot$ FoF haloes. Restricting the analysis to haloes well resolved within their virial radii, however, shows that the same haloes are identified by both algorithms and that masses within the virial radii are identical. To assign simulated halo masses to observed galaxies based on abundance matching, we thus recommend using only simulated haloes resolved within their virial radii, preferably by at least 5000 particles to ensure both high resolution and negligible dynamical over-relaxation, and ranking the haloes by their virial masses.

4. Haloes with masses below 2×10^{11} $M_\odot$ were often not well resolved within their virial radii by our simulations. The FoF and HOP halo masses were offset by ~ 20 percent, and the dispersion in the mass differences was $\sigma(M_h) = \beta M_h$ with $\beta \sim 0.2 - 0.4$. FoF and HOP do not preserve the rank ordering of haloes by mass at this level, undermining the prediction of galaxy properties to much better than this level of accuracy when halo masses are assigned to galaxies by abundance matching. In this case, we suggest a lower limit to the error in a predicted galaxy property may be estimated by averaging the property and its variance over a Gaussian distribution in halo mass with $\beta = 0.2 - 0.4$. A halo property varying as $f(M_h) \sim M_h^\alpha$ will then have a relative uncertainty of at least $\sigma_f / \langle f \rangle \simeq |\alpha\beta|$.

5. We introduce a new method for identifying haloes based on a gridded dark matter density field, similar to the spherical overdensity method for N-body particles. Haloes are found on the gridded density field by identifying contiguous regions with overdensity above a given threshold level $\Delta_{\rm th}$. A practical benefit of the method is that it does not require the particle data to be saved from a simulation to find haloes, a particular advantage for massive simulations. For $\Delta_{\rm th} = 178$, the halo masses are about 30 percent lower than the FoF masses for the same indentified haloes, but the masses come into good agreement if the density threshold is lowered to $\Delta_{\rm th} = 80$. Similarly, for $\Delta_{\rm th} = 178$ the **GADGET-3** halo counts are offset by ~ 30 percent below the halo mass function of Tinker et al. (2008), and by ~ 50 percent for the **Enzo** haloes. Using instead $\Delta_{\rm th} = 80$ brings the counts into good agreement with Tinker et al. (2008).

Our main results concerning the gas properties are:

1. GADGET-3 and Enzo identify similar halo structures for a given halo mass for haloes with well resolved virial cores. For our simulations, these correspond to haloes with masses exceeding 2×10^{11} M$_\odot$. The dark matter density profiles averaged over the haloes agree typically to 10–30 percent over radii $r_V < r < 8$ Mpc (comoving) from the halo centres of mass. The mode of gas removal, however, affects the dark matter density profile in the secondary infall region beyond the virial radius by a few tens of percent. The internal velocity dispersion of the gas in the haloes is found to agree closely between the GADGET-3 and Enzo haloes. The peculiar velocities of the haloes themselves are poorly converged with box size, as expected since the velocity power spectrum has signficant power on scales in excess of 100 Mpc, driving large scale flows.

2. There are pronounced differences in the circumgalactic gas properties between the GADGET-3 and Enzo haloes as a consequence of the differences in the treatement of unresolved rapidly cooling gas. The GADGET-3 simulation converts most of the gas into collisionless particles inside the haloes. The mass-weighted temperature of the remaining gas within the virial radius is substantially higher than that of the gas in the corresponding Enzo haloes. A broad high temperature region extending over 2–3 virial radii develops around the GADGET-3 haloes. The Enzo simulations suppress the rapid cooling of gas because of their restricted spatial resolution. The hot regions of the haloes are more compact than in the GADGET-3 haloes, and develop a multiphase medium including cooling gas within the virial cores. We conclude that any predictions of the physical properties of the circumgalactic gas may be made only within the context of a specific gas removal prescription.

3. Outside the turn-around radii, the gas density and temperature agree to 30 percent between comoving box sizes of 30 and 60 Mpc, and to 40 percent between the GADGET-3 and Enzo simulations, without reaching better than 10 percent agreement until as far out as several turn-around radii. The physical properties of the gas at these distances may be reliably computed, although the treatment of rapidly cooling gas is still a limiting factor in the accuracy of the predictions out to several turn-around radii.

4. The wind model we implemented in a GADGET-3 simulation affects the circumgalactic gas, slowing the accretion but not producing outflow in terms of the peculiar velocity. It increases the extent of the hot haloes, doubling the gas temperature compared with the windless model beyond the turn-around radius, while the gas density converges to the cosmic mean value.

5. A halo mass offset of ± 0.1 dex compared with a population of observed galaxies will introduce errors in the predicted neutral hydrogen density, gas temperature and gas velocities of 10–20 percent outside the turn-around radii of the haloes. An offset of ± 0.3 dex increases the errors to 20–40 percent. The high tolerance of the properties of the intergalactic gas near the haloes to the uncertain halo mass should permit predictions of the H I absorption line properties of the gaseous environment of galaxies to good accuracy. Large discrepancies with observations would suggest the influence of a wind.

We conclude that galactic mass haloes with essentially the same dark matter properties are reproduced at $2 < z < 5$ by GADGET-3 and Enzo IGM simulations in 30 Mpc comoving volumes and a spatially resolved Jeans length. Although the masses assigned to haloes are sensitive to the halo finding algorithm, the different halo finding algorithms we consider identify largely the same systems for halo masses exceeding $\sim 4 \times 10^{10}$ M$_\odot$, and essentially identical systems for masses exceeding $\sim 2 \times 10^{11}$ M$_\odot$. The physical properties of the intergalactic gas surrounding the GADGET-3 and Enzo haloes with masses exceeding $\sim 2 \times 10^{11}$ M$_\odot$ are found to agree to 30–40 percent beyond the turn-around radii. At smaller radii, the GADGET-3 and Enzo haloes show substantial differences in the gas density and temperature as a consequence of the differences in the treatment of rapidly cooling gas on spatially unresolved scales. We thus conclude that generic IGM simulations are able to make accurate predictions for the intergalactic gas properties of observed moderate redshift galaxies beyond the halo turn-around radii, but the properties of circumgalactic gas are highly dependent on the choices of star formation and feedback implementation.

ACKNOWLEDGMENTS

This work used the DiRAC Data Analytic system at the University of Cambridge, operated by the University of Cambridge High Performance Computing Service on behalf of the STFC DiRAC HPC Facility (www.dirac.ac.uk). This equipment was funded by BIS National E-infrastructure capital grant (ST/K001590/1), STFC capital grants ST/H008861/1 and ST/H00887X/1, and STFC DiRAC Operations grant ST/K00333X/1. DiRAC is part of the National E-Infrastructure. Additional computations were performed on facilities funded by an STFC Rolling-Grant and consolidated grant. AM thanks B. Smith for information regarding details of the operations of yt (http://yt-project.org), used for analysing some of the ENZO simulations, and J. Cohn and M. White for helpful conversations. JSB acknowledges the support of a Royal Society University Research Fellowship. ERT is supported by an STFC consolidated grant. We thank V. Springel for making GADGET-3 available. Computations described in this work were performed using the Enzo code developed by the Laboratory for Computational Astrophysics at the University of California in San Diego (http://lca.ucsd.edu).

REFERENCES

Becker G. D., Bolton J. S., Haehnelt M. G., Sargent W. L. W., 2011, MNRAS, 410, 1096
Behroozi P. S., Wechsler R. H., Conroy C., 2013, ApJ, 770, 57
Bertschinger E., 1985, ApJS, 58, 39
Bhattacharya S., Heitmann K., White M., Lukić Z., Wagner C., Habib S., 2011, ApJ, 732, 122
Birnboim Y., Dekel A., 2003, MNRAS, 345, 349
Bolton J. S., Haehnelt M. G., Viel M., Springel V., 2005, MNRAS, 357, 1178
Bryan G. L., Norman M. L., O'Shea B. W., Abel T., Wise J. H., Turk M. J., Reynolds D. R., Collins D. C., Wang P., Skillman S. W., Smith B., + 2014, ApJS, 211, 19
Cohn J. D., White M., 2008, MNRAS, 385, 2025
Cole S., Lacey C., 1996, MNRAS, 281, 716

Creasey P., Theuns T., Bower R. G., 2013, MNRAS, 429, 1922
Crighton N. H. M., Bielby R., Shanks T., Infante L., Bornancini C. G., Bouché N., Lambas D. G., Lowenthal J. D., Minniti D., Morris S. L., Padilla N., Péroux C., Petitjean P., Theuns T., + 2011, MNRAS, 414, 28
Dalla Vecchia C., Schaye J., 2012, MNRAS, 426, 140
Davis M., Efstathiou G., Frenk C. S., White S. D. M., 1985, ApJ, 292, 371
Dekel A., Silk J., 1986, ApJ, 303, 39
Efstathiou G., 1992, MNRAS, 256, 43P
Einasto J., Klypin A. A., Saar E., Shandarin S. F., 1984, MNRAS, 206, 529
Eisenstein D. J., Hut P., 1998, ApJ, 498, 137
Franx M., Illingworth G. D., Kelson D. D., van Dokkum P. G., Tran K.-V., 1997, ApJ, 486, L75
Frenk C. S., White S. D. M., Davis M., Efstathiou G., 1988, ApJ, 327, 507
Fujita A., Mac Low M.-M., Ferrara A., Meiksin A., 2004, ApJ, 613, 159
Genzel R., Newman S., Jones T., Förster Schreiber N. M., Shapiro K., Genel S., Lilly S. J., Renzini A., Tacconi L. J., + 2011, ApJ, 733, 101
Haardt F., Madau P., 2012, ApJ, 746, 125
Heitmann K., Lukić Z., Fasel P., Habib S., Warren M. S., White M., Ahrens J., Ankeny L., Armstrong R., O'Shea B., Ricker P. M., Springel V., Stadel J., Trac H., 2008, Computational Science and Discovery, 1, 015003
Hennawi J. F., Prochaska J. X., Burles S., Strauss M. A., Richards G. T., Schlegel D. J., Fan X., Schneider D. P., Zakamska N. L., Oguri M., Gunn J. E., Lupton R. H., Brinkmann J., 2006, ApJ, 651, 61
Hinshaw G., Larson D., Komatsu E., Spergel D. N., Bennett C. L., Dunkley J., Nolta M. R., Halpern M., + 2013, ApJS, 208, 19
Kereš D., Katz N., Weinberg D. H., Davé R., 2005, MNRAS, 363, 2
Klypin A., Prada F., Yepes G., Hess S., Gottlober S., 2013, ArXiv e-prints, 1310.3740
Knebe A., Pearce F. R., Lux H., Ascasibar Y., Behroozi P., Casado J., Moran C. C., Diemand J., + 2013, MNRAS, 435, 1618
Kravtsov A. V., Berlind A. A., Wechsler R. H., Klypin A. A., Gottlöber S., Allgood B., Primack J. R., 2004, ApJ, 609, 35
Lacey C., Cole S., 1994, MNRAS, 271, 676
Larson R. B., 1974, MNRAS, 169, 229
Lukić Z., Reed D., Habib S., Heitmann K., 2009, ApJ, 692, 217
Mac Low M.-M., McCray R., Norman M. L., 1989, ApJ, 337, 141
Mathews W. G., Baker J. C., 1971, ApJ, 170, 241
Meiksin A., 2011, MNRAS, 417, 1480
Meiksin A., White M., 2004, MNRAS, 350, 1107
Meiksin A. A., 2009, Reviews of Modern Physics, 81, 1405
Moster B. P., Somerville R. S., Maulbetsch C., van den Bosch F. C., Macciò A. V., Naab T., Oser L., 2010, ApJ, 710, 903
Murray N., Quataert E., Thompson T. A., 2005, ApJ, 618, 569
Okamoto T., Gao L., Theuns T., 2008, MNRAS, 390, 920
Onions J., Knebe A., Pearce F. R., Muldrew S. I., Lux H., Knollmann S. R., Ascasibar Y., Behroozi P., Elahi P., Han J., Maciejewski M., Merchán M. E., Neyrinck M., Ruiz A. N., Sgró M. A., Springel V., Tweed D., 2012, MNRAS, 423, 1200
Oppenheimer B. D., Davé R., 2008, MNRAS, 387, 577
O'Shea B. W., Nagamine K., Springel V., Hernquist L., Norman M. L., 2005, ApJS, 160, 1
Pettini M., Shapley A. E., Steidel C. C., Cuby J.-G., Dickinson M., Moorwood A. F. M., Adelberger K. L., Giavalisco M., 2001, ApJ, 554, 981
Pettini M., Steidel C. C., Adelberger K. L., Dickinson M., Giavalisco M., 2000, ApJ, 528, 96
Press W. H., Davis M., 1982, ApJ, 259, 449
Prochaska J. X., Hennawi J. F., Simcoe R. A., 2013, ApJ, 762, L19
Quider A. M., Shapley A. E., Pettini M., Steidel C. C., Stark D. P., 2010, MNRAS, 402, 1467
Rakic O., Schaye J., Steidel C. C., Booth C. M., Dalla Vecchia C., Rudie G. C., 2013, MNRAS, 433, 3103
Rakic O., Schaye J., Steidel C. C., Rudie G. C., 2012, ApJ, 751, 94
Reed D. S., Bower R., Frenk C. S., Jenkins A., Theuns T., 2007, MNRAS, 374, 2
Rudie G. C., Steidel C. C., Trainor R. F., Rakic O., Bogosavljević M., Pettini M., Reddy N., Shapley A. E., Erb D. K., Law D. R., 2012, ApJ, 750, 67
Sawala T., Frenk C. S., Fattahi A., Navarro J. F., Bower R. G., Crain R. A., Dalla Vecchia C., Furlong M., Jenkins A., McCarthy I. G., Qu Y., Schaller M., Schaye J., Theuns T., 2014, ArXiv e-prints, 1404.3724
Scholz T. T., Walters H. R. J., 1991, ApJ, 380, 302
Spitzer L., 1987, Dynamical evolution of globular clusters. Princeton, NJ, Princeton University Press, 1987
Springel V., 2005, MNRAS, 364, 1105
Springel V., Hernquist L., 2003, MNRAS, 339, 289
Steidel C. C., Erb D. K., Shapley A. E., Pettini M., Reddy N., Bogosavljević M., Rudie G. C., Rakic O., 2010, ApJ, 717, 289
Steidel C. C., Giavalisco M., Pettini M., Dickinson M., Adelberger K. L., 1996, ApJ, 462, L17
Tinker J., Kravtsov A. V., Klypin A., Abazajian K., Warren M., Yepes G., Gottlöber S., Holz D. E., 2008, ApJ, 688, 709
Tittley E. R., Meiksin A., 2007, MNRAS, 380, 1369
Trainor R. F., Steidel C. C., 2012, ApJ, 752, 39
Trenti M., Smith B. D., Hallman E. J., Skillman S. W., Shull J. M., 2010, ApJ, 711, 1198
Vale A., Ostriker J. P., 2006, MNRAS, 371, 1173
Velliscig M., van Daalen M. P., Schaye J., McCarthy I. G., Cacciato M., Le Brun A. M. C., Dalla Vecchia C., 2014, ArXiv e-prints, 1402.4461
Viel M., Haehnelt M. G., Springel V., 2004, MNRAS, 354, 684
Warren M. S., Quinn P. J., Salmon J. K., Zurek W. H., 1992, ApJ, 399, 405
Watson W. A., Iliev I. T., D'Aloisio A., Knebe A., Shapiro P. R., Yepes G., 2013, MNRAS, 433, 1230
Weiner B. J., Coil A. L., Prochaska J. X., Newman J. A., Cooper M. C., Bundy K., Conselice C. J., Dutton A. A., Faber S. M., Koo D. C., Lotz J. M., Rieke G. H., Rubin K. H. R., 2009, ApJ, 692, 187
White M., 2002, ApJS, 143, 241

APPENDIX A: MINIMUM HALO MASS IN IGM SIMULATIONS

In this appendix, we show the simulations used in this work are adequate for resolving and selecting galaxy haloes of mass exceeding 10^{11} M$_\odot$, matching observed galaxies with associated H I absorption measurements.

We first show the haloes will not be overly dynamically relaxed. A halo of mass M_h comprised of N particles will have a median dynamical relaxation time of $t_{\rm rh} \simeq [0.138N/\log(0.4N)](r_h^3/GM_h)^{1/2}$ (Spitzer 1987), where r_h is the half mass radius. In terms of the Hubble time $t_{\rm H} = 2/3H(z)$ for a virialized halo of overdensity $18\pi^2$ compared with the cosmic mean density, the criterion for negligible two-body relaxation is

$$\frac{t_{\rm rh}}{t_{\rm H}} \simeq \frac{2^{1/2}}{4\pi}\frac{0.138N}{\log(0.4N)}\left[1+\frac{\Omega_v}{\Omega_m(1+z)^3}\right]^{1/2} \gg 1, \qquad \text{(A1)}$$

or $N \gg 310$ for $z \gg 1$ (and $N \gg 136$ at $z = 0$). In terms of the simulations presented here, this corresponds to the halo mass limit $M_h = N(m_c + m_g) \gg 2.4 \times 10^9$ M$_\odot$ for $z \gg 1$ (and $M_h \gg 1.0 \times 10^9$ M$_\odot$ at $z = 0$). A safer lower limit to ensure negligible over-relaxation is $t_{\rm rh}/t_{\rm H} > 10$, corresponding to minimum particle numbers per halo of $N_{\rm min} > 4880$ for $z \gg 1$ (and $N_{\rm min} > 2330$ at $z = 0$). This corresponds to a minimal halo mass of $M_{h,\rm min} = N_{\rm min}(m_c + m_g) = 3.8 \times 10^{10}$ M$_\odot$ to ensure negligible over-relaxation effects for $z \gg 1$. This is comparable to the minimum resolvable halo mass in the `Enzo` simulations.

These estimates are similar to those based on convergence tests on halo properties. Using `GADGET` simulations of increasing mass resolution with identical initial conditions, Trenti et al. (2010) find the masses of FoF haloes identifiable in different resolution simulations have typical uncertainties of $\Delta M_h/M_h \sim 1.5/N^{1/3}$, a dependence they attribute to errors in the number of particles in the halo peripheries. On this criterion, achieving a halo mass precision of 10 percent requires $N > 3000$ particles, or $M_h > 2.3 \times 10^{10}$ M$_\odot$. Bhattacharya et al. (2011) suggest halo masses are biased high in N-body simulations and are more accurate if corrected by the factor $M_c/M = [1.0 - 0.04(\epsilon/650\,{\rm kpc})](1 - N^{-0.65})$, where ϵ is the force resolution in (comoving) kpc. Applied to our `GADGET-3` and `Enzo` runs with $N = N_{\rm min}$, this corresponds to a correction by 0.5 and 1 percent, respectively. Since these are smaller than the accuracy we require, we do not include this correction. We conclude that the haloes we focus on in this paper should be free of resolution, force error and over-relaxation systematics.

Finally, Fig. A1 compares the masses of the haloes identified using the grid based halo finder for two different density thresholds with the masses of the matching haloes identified with FoF. This demonstrates that the increase in the counts of the FoF haloes in a given mass bin in Fig. 5 compared with the GHF haloes arises primarily from the greater extents of the FoF haloes. These enclose more mass and so shift the haloes to a higher mass bin than the corresponding GHF haloes found using $\Delta_{\rm th} = 178$. As found when comparing FoF and HOP halo counts, the scatter shows that the rankings of the haloes by mass is not preserved.

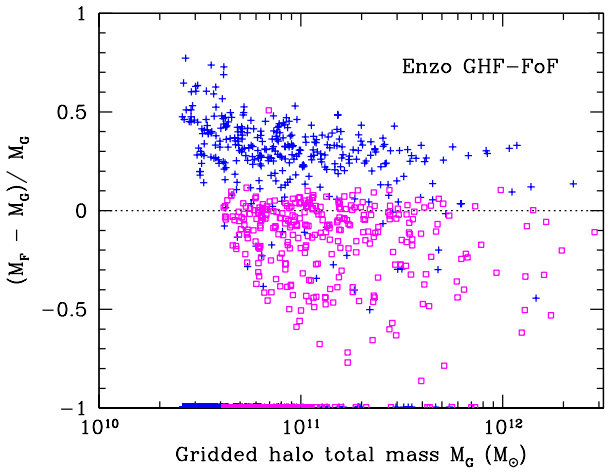

Figure A1. Fractional halo mass differences between N-body haloes identified using FoF (M_F) and haloes found using the grid based halo finding algorithm (M_G), for the `Enzo` simulation E30_512 at $z = 3$. The blue crosses show the results when a threshold density of $\Delta_{\rm th} = 178$ is used to identify the haloes in the grid halo finder, and the magenta open squares show results for $\Delta_{\rm th} = 80$. The masses identified by the two approaches come into good agreement when the haloes on the gridded density field are grown to the lower overdensity threshold. The points along the bottom axis indicate unmatched haloes.